Simulation of atrial fibrillation in a non-ohmic propagation model with dynamic gap junctions

Ariane Saliani,[1,2] Subhamoy Biswas,[1,2] and Vincent Jacquemet[1,2,a]

[1] *Institute of Biomedical Engineering, Department of Pharmacology and Physiology, Faculty of Medicine, Université de Montréal, C.P. 6128, succ. Centre-ville, Montreal (QC), H3C 3J7 Canada*

[2] *Research Center, Hôpital du Sacré-Coeur, CIUSSS du Nord-de-l'Île-de-Montréal, 5400 boul. Gouin Ouest, Montreal (QC), H4J 1C5 Canada*

ABSTRACT:

Gap junctions exhibit nonlinear electrical properties that have been hypothesized to be relevant to arrhythmogenicity in structurally remodeled tissue. Large-scale implementation of gap junction dynamics in 3D propagation models remains challenging. We aim to quantify the impact of nonlinear diffusion during episodes of arrhythmias simulated in a left atrial model. Homogenization of conduction properties in the presence of nonlinear gap junctions was performed by generalizing a previously developed mathematical framework. A monodomain model was solved in which conductivities were time-varying and depended on transjunctional potentials. Gap junction conductances were derived from a simplified Vogel-Weingart model with first-order gating and adjustable time constant. A bilayer interconnected cable model of the left atrium with 100 μm resolution was used. The diffusion matrix was recomputed at each time step according to the state of the gap junctions. Sinus rhythm and atrial fibrillation episodes were simulated in remodeled tissue substrates. Slow conduction was induced by reduced coupling and by diffuse or stringy fibrosis. Simulations starting from the same initial conditions were repeated with linear and nonlinear gap junctions. The discrepancy in activation times between the linear and nonlinear diffusion models was quantified. The results largely validated the linear approximation for conduction velocities > 20 cm/s. In very slow conduction substrates, the discrepancy accumulated over time during atrial fibrillation, eventually leading to qualitative differences in propagation patterns, while keeping the descriptive statistics such as cycle lengths unchanged. The discrepancy growth rate was increased by impaired conduction, fibrosis, conduction heterogeneity, lateral uncoupling, fast gap junction time constant, and steeper action potential duration restitution.

---

a)Electronic mail: vincent.jacquemet@umontreal.ca

Propagation of the electrical impulse in cardiac tissue is often modeled by reaction–diffusion equations. The rationale behind the linear diffusion model is that current flow between cardiac cells passes through intercellular connections called gap junctions that act approximately as passive resistors. Experimental electrophysiological recordings have demonstrated that gap junctions exhibit nonlinear time-dependent dynamics when the transjunctional potential is large. This criterion is met in tissues with very slow conduction, which typically occurs in pathological, arrhythmogenic conditions. This raises the question of whether nonlinear diffusion plays a role during an arrhythmia. In this paper, linear and nonlinear diffusion are compared to assess the validity of the linear gap junction hypothesis in the context of atrial fibrillation.

———————————————

I. INTRODUCTION

Myocardial cells are connected to their neighbors through small channels called gap junctions. The diffusion of ions through these gap junctions generates a current that couples the electrical activity of neighboring myocytes.[1] A gap junction is composed of two hemi-channels formed from the assembly of six proteins (connexins, abbreviated Cx). These channels open or close in response to factors including voltage and calcium ion concentration.[2]

In the atria, propagation of the electrical impulse is predominantly mediated by Cx40 and Cx43 gap junctions.[3–5] The majority of gap junctions are located along the longitudinal axis of the cells.[6] Propagation is then faster in the longitudinal direction than in the transverse direction. Furthermore, gap junctions present a larger resistance than the cytoplasm, thus slowing propagation and causing a non-uniform, discontinuous propagation and a stair-step shaped spatial profile of membrane potential.[5,7,8] During atrial fibrillation, this non-uniform propagation may ultimately cause conduction blocks[4] which may originate from the remodeling of gap junctions.[9,10] There is considerable evidence that cardiac injury results in gap junction remodeling, marked by loss or lateralization of gap junctions, which in turn is associated with decreases in conduction velocity and increased susceptibility to arrhythmias.[11–15]

In first approximation, the gap junction current-voltage relationship is linear. After

homogenization, the propagation equation becomes the widely-used monodomain reaction-diffusion equation.[16–19] When the potential across the gap junction is large, however, its behavior becomes nonlinear and the kinetics of opening and closing of the channel enters in action.[5,20] This happens when conduction is very slow and the cell-to-cell activation delay is long. The first approach for simulating nonlinear diffusion is phenomenological. For instance, fractional,[21–23] porous-medium,[24] deformable-medium,[25] electro-mechanical[26,27] and thermo-electric coupled[28–30] diffusion have been proposed to generalize the monodomain equation. An alternative is the bottom-up approach. Dynamical models of the kinetics of the gap junction[20,31–33] including its calcium-dependent gating[34] have been developed. Microstructural propagation models with subcellular discretization were built upon these gap junction models to study the influence of nonlinear gap junctions on propagation.[8,35,36] The discretization in these models is sufficient to investigate intracellular ion flow and the role of intercalated discs.[26,37] Ephaptic coupling can be introduced in a conduction model to provide an extracellular pathway that may compensate for low gap junction expression.[38,39] Finally, another approach is to reconstruct the geometry of the intracellular medium including the pores (gap junctions) that connect neighboring cells.[16,19,40,41] This requires extremely fine discretization at the scale of a single gap junction. New simulation techniques may be needed to help alleviate the computational load.[42,43]

Physiologists have postulated that gap junction nonlinear dynamics might contribute to conduction slowing and to the maintenance of reentrant arrhythmia.[33,44] Testing this hypothesis *in silico* necessitates an organ-scale model in two or three dimensions and therefore some form of homogenization to limit computational requirements (e.g., 100 μm instead of 5 μm discretization). Hurtado et al.[36] paved the way in that direction by deriving a one-dimensional mathematical formulation of non-ohmic conduction that incorporates the nonlinear current-voltage relationship of gap junctions.

In this paper, the Hurtado formalism is extended to two/three dimensions to simulate atrial fibrillation in models with and without gap junction nonlinearity. This extension will be facilitated by the use of an interconnected cable model of the left atrium, whose mesh structure reflects the arrangement of fibers. Longitudinal and transverse coupling will therefore be easily identified and separated. Our approach is top-down in the sense that it starts from a given macroscopic linear diffusion model and creates nonlinear models that are equivalent to the linear one in the small transjunctional potential limit. In addition,

a simplified first-order kinetics model of gap junction gating is proposed to investigate the effect of time constants.

II. METHODS

A. Nonlinear conductances in series

First, consider longitudinal propagation in a one-dimensional strand of cells. Each cell has length L_{cell} and cross-section area S_{cell}. The conductivity within the cell (cytoplasmic) is denoted by σ_c. The conductance of the intracellular medium for longitudinal current flow is written as

$$G_c = \frac{\sigma_c S_{\text{cell}}}{L_{\text{cell}}} \ .$$ (1)

The potential difference between both ends of the interior of the cell is denoted by V_c. The longitudinal current I flowing through the cell is therefore $I = G_c V_c$. Notations are illustrated in Fig. 1.
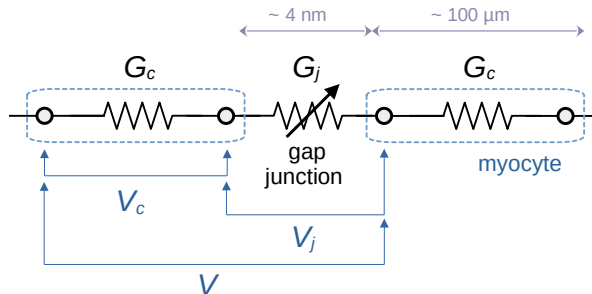

FIG. 1. Model of a strand of cells. Illustration of the notations for the conductances and the potential differences.

Assume that there is a density ρ_{gap} of gap junctions at the extremities of the cell and that each gap junction has a non-linear conductance $g_j(V_j)$, where V_j is the junctional potential (potential difference between the two sides of the gap junction). The total gap junction conductance between two consecutive cells is

$$G_j(V_j) = \rho_{\text{gap}} S_{\text{cell}}\, g_j(V_j)$$ (2)

and the current flowing through the gap junctions is $I = G_j(V_j) \cdot V_j$.

5

The equivalent conductance is defined as the non-linear conductance function $G(V)$ depending on $V = V_c + V_j$ such that $G(V) \cdot V = I$. Because $I = G_c \cdot (V - V_j)$, we have:

$$V_j = \left(1 - \frac{G(V)}{G_c}\right) V \ . \tag{3}$$

Substituting this relation in $G(V) \cdot V = G_j(V_j) \cdot V_j = I$, we obtain the formula for conductances in series

$$G(V)^{-1} = G_c^{-1} + G_j(V_j)^{-1} \ , \tag{4}$$

where V_j is a function of V given by (3). This is a nonlinear implicit definition of $G(V)$, assuming that the function $G_j(V_j)$ is known.

B. Equivalent conductivity with nonlinear gap junctions

The equivalent conductivity $\sigma(V)$ of the cell strand is defined by the relation

$$G(V) = \frac{\sigma(V) S_{\text{cell}}}{L_{\text{cell}}} \tag{5}$$

which allows rescaling the equations:

$$\frac{G(V)}{G_c} = \frac{\sigma(V)}{\sigma_c} \qquad \text{and} \qquad \frac{G_j(V_j)}{G_c} = \rho_{\text{gap}} L_{\text{cell}} \frac{g_j(V_j)}{\sigma_c} \ . \tag{6}$$

Equation (4) becomes:

$$\sigma(V)^{-1} = \sigma_c^{-1} + \left(\rho_{\text{gap}} L_{\text{cell}} \, g_j(V_j)\right)^{-1} \ . \tag{7}$$

Since $\rho_{\text{gap}} L_{\text{cell}}$ is not known, it may be more convenient to express the equivalent conductivity in terms of $\sigma_0 = \sigma(0)$ which corresponds to the conductivity of the tissue when gradients are small ($V \to 0$) and current flows follow Ohm's law:

$$\rho_{\text{gap}} L_{\text{cell}} = \frac{1}{g_j(0) \cdot (\sigma_0^{-1} - \sigma_c^{-1})} \ . \tag{8}$$

Then, after defining the normalized conductance $\hat{g}_j(V_j) = g_j(V_j)/g_j(0)$, Eq. (7) becomes:

$$\frac{\sigma(V)}{\sigma_c} = \frac{\hat{g}_j}{\frac{\sigma_c}{\sigma_0} - 1 + \hat{g}_j} \qquad \text{where} \qquad \hat{g}_j = \hat{g}_j\left(\left(1 - \frac{\sigma(V)}{\sigma_c}\right) V\right) \ . \tag{9}$$

6

Practically, σ_0 comes from a previously developed continuous ohmic model; σ_c is taken from experimental data ($\sigma_c > \sigma_0$); $\hat{g}_j$ is derived from a gap junction model (see next Subsection). Since $\hat{g}_j(0) = 1$, we have $\sigma(0) = \sigma_0$ as expected. When $V \neq 0$, $\sigma(V)$ is first approximated by σ_0 and fixed-point iterations are used to solve the nonlinear equation.

C. Gap junction model

Vogel and Weingart proposed a nonlinear gap junction model with four-state Markov model of channel gating.[20] We developed a simplified model based on the instantaneous gap junction conductance $g_{\text{inst}}(V_j)$, the steady-state conductance $g_{\text{ss}}(V_j)$, and a first-order gate p_{open} with a fixed time constant τ_{gap}:

$$\hat{g}_j(V_j) = g_{\text{inst}}(V_j) \ p_{\text{open}}(t) \tag{10}$$

$$\frac{\mathrm{d}p_{\text{open}}}{\mathrm{d}t} = \frac{g_{\text{ss}}(V_j)/g_{\text{inst}}(V_j) - p_{\text{open}}}{\tau_{\text{gap}}} \tag{11}$$

The functions $g_{\text{inst}}(V_j)$ and $g_{\text{ss}}(V_j)$ can be measured experimentally, as well as τ_{gap}. We used the functions derived from the Vogel-Weingart model with the parameters from Brown et al.[8] The gates were assumed to be open at initial time: $p_{\text{open}}(0) = 1$.

In the limit $\tau_{\text{gap}} \to 0$, the gate is always at steady-state $p_{\text{open}} = g_{\text{ss}}/g_{\text{inst}}$, so that $\hat{g}_j(V_j) = g_{\text{ss}}(V_j)$. In the limit $\tau_{\text{gap}} \to \infty$, we always have $p_{\text{open}}(t) = 1$ and $\hat{g}_j(V_j) = g_{\text{inst}}(V_j)$. These limit cases correspond to the Hurtado et al. model.[36]

D. Anatomical model of the left atrium

The one-dimensional Hurtado et al. model[36] was extended to three dimensions by exploiting the structure of our bilayer interconnected cable model of the left atrium.[45–47] The general modeling approach is illustrated in Fig. 2. The geometrical model is composed of a set of longitudinal, transverse and transmural cables intertwined like fabric threads, with a spatial resolution of 100 μm. A computational node is typically part of three orthogonal cables. Each cable is handled like a strand of cells following the approach of the preceding subsections. A segment of a cable denotes the connection between two neighboring computational nodes and is associated with a gap junction state (a variable p_{open}). Overall, the

atrial myocardium is represented as a network of nonlinear resistors, each of which is either longitudinal or transverse.
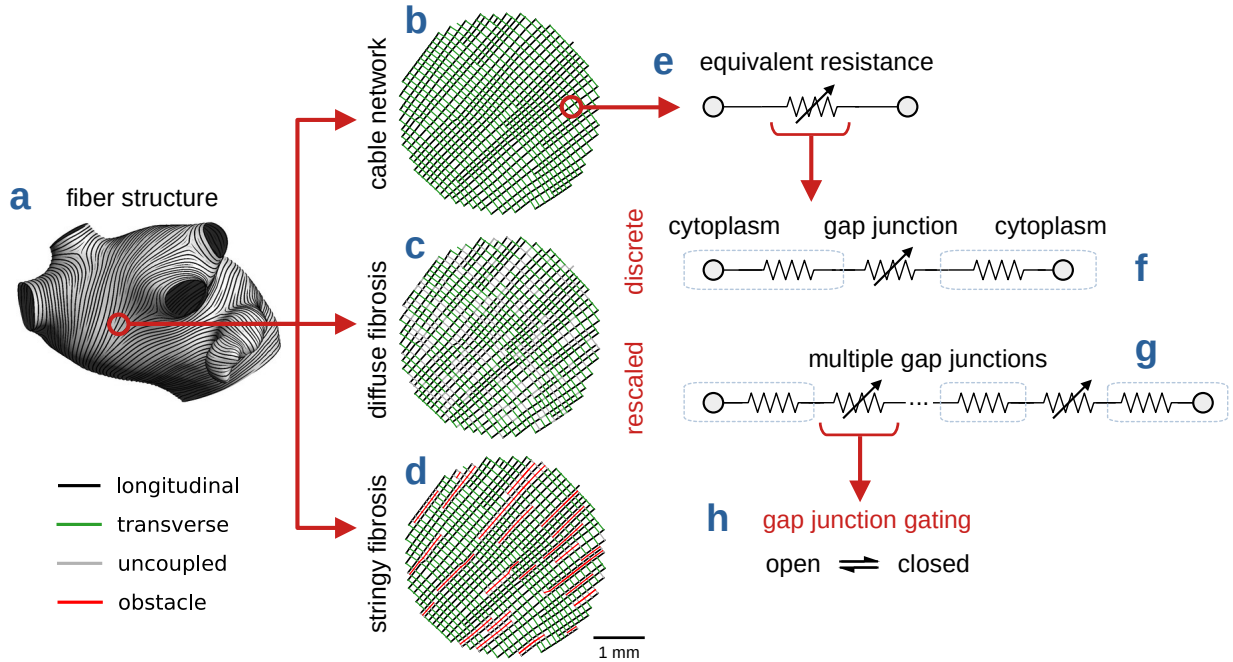

FIG. 2. Modeling approach: (a) geometric model of the left atrium with the fiber orientation of the epicardial layer; (b) illustration of the longitudinal and transverse cables; (c) diffuse fibrosis introduced by random uncoupling; (d) stringy fibrosis generated by removal of consecutive transverse gap junctions along longitudinal cables; (e) equivalent resistance between computational nodes; (f) discrete formula [Eq. (12)] for computing the cell-to-cell potential difference; (g) rescaled formula [Eq. (13)]; (h) gap junction model with two-state gate.

A possibly nonuniform conductivity value σ_0 is assigned to each segment of the cables in order to form a baseline propagation model with linear diffusion. Anisotropy is specified by assigning a larger σ_0 to longitudinal cables. Nonlinear diffusion is simulated by allowing conductivities to change over time according to the current state of the gap junctions. Finally, the monodomain equation is solved using the numerical methods presented in Saliani et al.[46] The solver outputs the membrane potential $V_m(x, t)$ along each cable at time t, with x being the curvilinear coordinate along the cable.

E. Algorithm for updating conductivities

The simulation of nonlinear diffusion requires to update the conductivity σ of cable segments (initially set to σ_0) and to recompute the finite-difference diffusion matrix. This

update is performed every $\Delta t = 0.1$ ms according to the following steps:

1. The cell-to-cell potential difference V is computed in each cable segment. The discrete formula consists in calculating V as the difference in membrane potential V_m between two consecutive nodes i and $i+1$ of the cable:

$$V \approx V_m^{(i+1)} - V_m^{(i)} \tag{12}$$

   The monodomain assumption that the gradient of the intracellular and the transmembrane potentials are approximately the same is implied. If cable discretization does not correspond to cell size, V could be rescaled:

$$V \approx \left(V_m^{(i+1)} - V_m^{(i)} \right) \cdot \frac{L_{\mathrm{cell}}}{d_{i,\,i+1}} \,, \tag{13}$$

   where $d_{i,\,i+1}$ is the distance between nodes i and $i+1$, i.e., the length of the cable segment. Because of cell shape, the parameter L_{cell} may take a different value in longitudinal and transverse cables. The application of Eq. (13) will be referred to as scaling. Simulations will be performed with scaling or using the discrete formula.

2. The relationship $\hat{g}_j(V_j)$ is determined from Eq. (10) based on the current value of p_{open}. This approximation is valid when $\Delta t \ll \tau_{\mathrm{gap}}$. If $\tau_{\mathrm{gap}} = 0$, the function $\hat{g}_j(V_j)$ is set to $g_{\mathrm{ss}}(V_j)$, and if $\tau_{\mathrm{gap}} = \infty$, the function $\hat{g}_j(V_j)$ is set to $g_{\mathrm{inst}}(V_j)$. For computational efficiency, lookup tables were used for these functions, as in previous works.[35]

3. For each cable segment, with V from step 1 and $\hat{g}_j$ from step 2, Eq, (9) is solved for σ by fixed-point iterations from $\sigma = \sigma_0$. The junctional potential is calculated as $V_j = (1 - \sigma/\sigma_c)V$. Iterations terminate when the residual is smaller than 10^{-4} mS/cm. More iterations were needed when σ_0 was smaller and when V was larger (typically 1 to 5 iterations; up to 15 in the worst case). The intracellular conductivity σ_c was set to 6.67 mS/cm.[36,48]

4. Forward Euler integration is applied to update p_{open} using V_j from step 3, unless $\tau_{\mathrm{gap}} = 0$ or ∞ in which case this step can be skipped.

5. The finite-difference diffusion matrix is updated for all cables.[46]

F.   Arrhythmogenic substrates

Two modified versions of the Courtemanche model[49] were used for membrane kinetics. The first parameter set (63% I_{CaL} inhibition, 65% I_{to} inhibition, 73% increase in I_{K1}) was based on experimental data by Workman et al.[50] and had a relatively flat action potential duration restitution curve. The second one (30% I_{CaL} inhibition, 80% I_{to} inhibition, 90% I_{Kur} inhibition, 50% increase in I_{Kr}), proposed by Jacquemet et al.,[51] reproduced the clinical restitution curve (with a slope close to 1) measured by Kim et al..[52] These models will be referred to as "Workman" and "Kim" respectively.

The longitudinal conductivity (σ_0) was set to 2, 1 or 0.5 mS/cm; the conductivity anisotropy ratio was 4. Transmural coupling was weak (0.1 mS/cm) to reflect wall thickness as far as a bilayer model allows.[53] Diffuse fibrosis was simulated by randomly uncoupling longitudinal and transverse cable segments (σ_0 was locally set to zero). Fibrosis density was 10%, 20% or 30% in the model with a longitudinal conductivity of 2 mS/cm. This gave a total of 12 substrates (2 membrane kinetics $\times$ 2 types of conduction slowing $\times$ 3 levels of structural remodeling).

In addition, substrates with stringy fibrosis were created. A set of linear obstacles aligned in the longitudinal direction, with Poisson-distributed length, were randomly generated as described previously.[46] These linear obstacles were formed by removing a set of consecutive transverse gap junctions along a longitudinal cable (Fig. 2d). The fibrosis distribution was characterized by the average length of obstacles (0.1, 1, 3 or 5 mm) and the fraction of decoupled connections (5 values from 10% to 30%), leading to 20 substrates with stringy fibrosis.

G.   Simulation protocols

Sinus rhythm was simulated by injecting intracellular current in the Bachmann's bundle region. Atrial fibrillation was initiated by generating 4 fibrillatory initial conditions (each with 4 phase singularities) using an eikonal-diffusion approach.[54,55]

For each of the 12 substrates and each of the 4 initial conditions, propagation was simulated for 1 s using linear gap junctions. Then, from the resulting state (defining the time origin $t = 0$), simulations were run for 5.3 s with each of the 7 variants of our simplified

10

Code	Model	L_{cell}	τ_{gap}
L	linear	–	–
D_0	nonlinear	no scaling	0
S_{iso}	nonlinear	100 μm	0
S_{aniso}	nonlinear	100 μm (long), 15 μm (trans)	0
D_2	nonlinear	no scaling	2 ms
D_5	nonlinear	no scaling	5 ms
D_∞	nonlinear	no scaling	∞

TABLE I. Gap junction models.

gap junction model (see Table I), leading to a total of $12 \times 4 \times 7 = 336$ simulations. These models differed by the time constant τ_{gap} and by the presence or absence of scaling applied to the cell-to-cell potential according to Eq. (13). The time interval between $t = 0$ and $t = 5$ s was used for the analysis. Exclusion of the preceding 1 s and the succeeding 0.3 s (> 1 cycle length) eliminated boundary effects. The same protocol was applied to the 20 stringy fibrosis substrates, but only with the Workman model and the S_{aniso} gap junction model, which gave $20 \times 4 = 80$ additional simulations.

H.   Comparison of activation maps

In each simulation, activation time series were identified at 10,135 nodes evenly spread over the epicardial surface using a threshold at -70 mV on the membrane potential. Activation time series were compared to those simulated from the same initial condition with the linear gap junction model (used as a reference). To quantify the time evolution of the difference between two time series $t_0, t_1, \ldots, t_n$ and $t_0^{\text{ref}}, t_1^{\text{ref}}, \ldots, t_m^{\text{ref}}$ of possibly different lengths, the mutual nearest neighbors between the two sets of activation times were identified (Fig. 3). The time difference $t_i - t_j^{\text{ref}}$ between mutual nearest neighbors t_i and t_j^{ref} was attributed to time t_j^{ref}. Some activation times were left unpaired. Over all simulations, the percentage of unpaired activation times was 0.94% (up to 7.6% in very slow substrates with the Kim model).

These data were accumulated over all nodes, generating a list of pairs $(t_j^{\text{ref}}, t_i - t_j^{\text{ref}})$. In order to uniformly sample this new signal, the root mean square of the discrepancies $t_i - t_j^{\text{ref}}$ was computed over a moving time window of duration 500 ms and steps of 10 ms. This discrepancy curve (which starts at zero by construction) will be used to monitor the

11

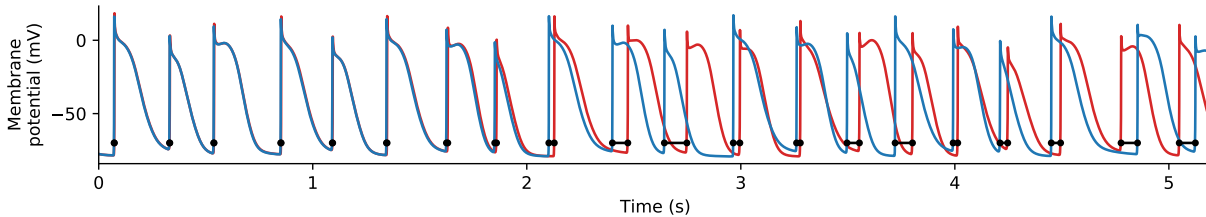divergence between the evolution of two simulations.

FIG. 3. Definition of the discrepancy in activation time between an activation time series (action potentials in red) and a reference time series (blue). The pairing of activation times through mutual nearest neighbors are shown in black.

To compare discrepancy curves, a robust measure of their slope was considered. If AUC is the area under the discrepancy curve in the time interval $[0, T]$, the discrepancy growth rate ω is defined as:

$$\omega = \frac{2 \cdot \text{AUC}}{T^2} \ . \tag{14}$$

If the discrepancy curve increases linearly from zero, ω is equal to the slope of the line. We used $T = 2.5$ s to avoid the regime where the discrepancy saturates; ω was expressed in ms/s.

III. RESULTS

A. Gap junction model

The main characteristics of the simplified gap junction model are presented in Fig. 4. The instantaneous normalized conductance g_{inst} is close to 1 when the junctional potential is smaller than 30 mV (panel A). The steady-state normalized conductance g_{ss} decreases significantly for larger junctional potentials. The time dependency of the normalized conductance $\hat{g}_j$ is illustrated by voltage clamp protocols (panel B). A step variation in junctional voltage results in an exponential decrease in normalized conductance with a relaxation time of τ_{gap}. These relationships are similar to experimental measurements by Lin et al.[5,33]

Both intracellular conductivity and gap junction conductance contribute to the equivalent tissue conductivity σ. Since only gap junctions exhibit nonlinearity, the effect of nonlinearity is reduced when a large part of the resistance comes from the intracellular medium (i.e. when σ_0 is large). Figure 4C shows that larger values of σ_0 (faster conduction velocity) result in
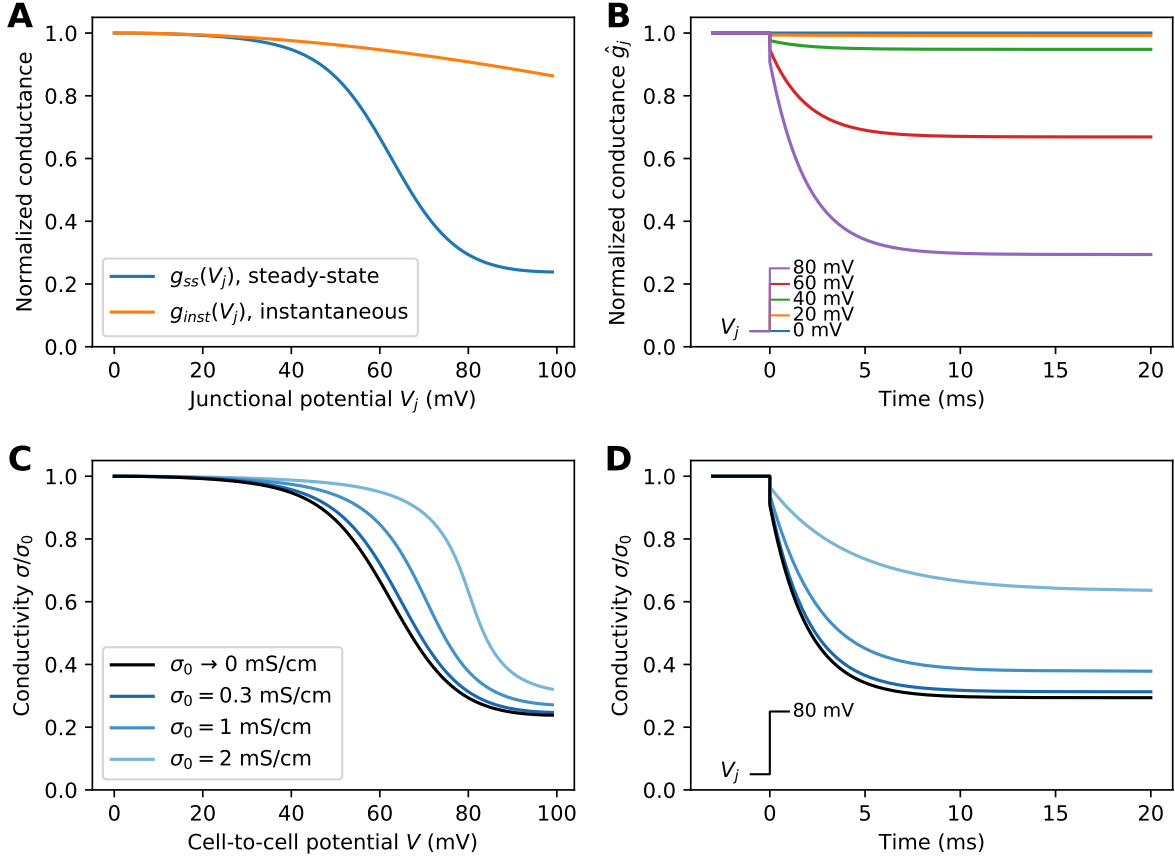
12

FIG. 4. Voltage clamp of the nonlinear gap junction model. (A) Instantaneous and steady-state normalized conductance function. (B) Normalized conductance $\hat{g}_j$ during a voltage clamp protocol consisting of a step in V_j from 0 to 20, 40, 60, 80 mV at time $t = 0$ in an isolated gap junction with $\tau_{\text{gap}} = 2$ ms. (C) Ratio of conductivity σ/σ_0 obtained by solving Eq. (9) where $\hat{g}_j$ is the steady-state normalized conductance g_{ss}, for four different color-coded values of σ_0. (D) With the same color code as panel C, simulated voltage clamp with a step of 80 mV ($\tau_{\text{gap}} = 2$ ms).

an increase of the ratio σ/σ_0 (it becomes closer to 1). In case of slow propagation ($\sigma_0 \to 0$) where gap junction resistance dominates, gap junction nonlinearity fully translates into equivalent conductivity nonlinearity. The same is observed on the time evolution of σ/σ_0 during a voltage clamp protocol (panel D). Note that the apparent time constant of the exponential decay is prolonged when σ_0 is larger.

B. Propagation in one dimension

Conduction velocity (CV) was measured in a uniform cable with different conductivity values and gap junction models (Fig. 5A for the Kim model) using linear regression of the

activation times in the middle third of the cable. Spatial resolution was either 100 μm or 15 μm to represent discrete propagation in the longitudinal or transverse direction. The theoretical relationship CV $\propto \sqrt{\sigma_0}$ was verified even for the lowest conductivities (< 0.1 mS/cm) with the finest discretization (transverse propagation). The effect on gap junction nonlinearity was $< 0.6\%$ even at the lowest conductivities. Conduction was slower with 100 μm discretization (longitudinal) relative to 15 μm. Nonlinear gap junctions resulted in further conduction slowing, particularly in conditions where CV < 10 cm/s. Effect size was about 2.1% when $\sigma_0 = 0.5$ mS/cm, and increased to 34% when $\sigma_0 = 0.1$ mS/cm (for $\tau_{\mathrm{gap}} = 0$). The larger the time constant τ_{gap}, the smaller the effect size.

The origin of conduction slowing caused by gap junction nonlinearity is illustrated in Fig. 5B, where the time evolution of the conductivity σ is shown for different values of σ_0 and τ_{gap}. During the depolarization phase of a cell, the junctional potential with respect to the next cell (still near its resting state) increased, leading to the progressive closure of the gates and therefore to a decrease of the conductivity σ. The gap junction recovered quickly after the next cell was depolarized. This gave a time window of < 2 ms during which conduction was depressed. Larger τ_{gap} values resulted in smaller but longer-lasting effects on σ. Note that at 5 cm/s, the time delay between the activation of consecutive cells is 2 ms, which explains the location of the peak in the left panel.

C. Sinus rhythm activation

Sinus rhythm was simulated in the 12 substrates with the different linear and nonlinear gap junction models of Table I. CV was computed by linear interpolation of activation times within 19,996 triangles obtained from a triangulation of the epicardial surface. The median CV over the surface was documented, which included both longitudinal and transverse propagation. Median CV ranged from 16 to 39 cm/s. The relative difference of CV between linear and nonlinear gap junction models was $< 1\%$ when CV > 25 cm/s and was in the interval from 1 to 5% when CV < 20 cm/s. These small percentages translated into a maximum delay of 0.5 ms for a total activation time of 202.7 ms when the longitudinal conductivity was $\sigma_0 = 2$ mS/cm. Longer delays (> 10 ms) were however observed in slow substrates where total activation times was up to 400 ms. The delay between the linear and the nonlinear models tended to be proportional to the length of the pathway from the
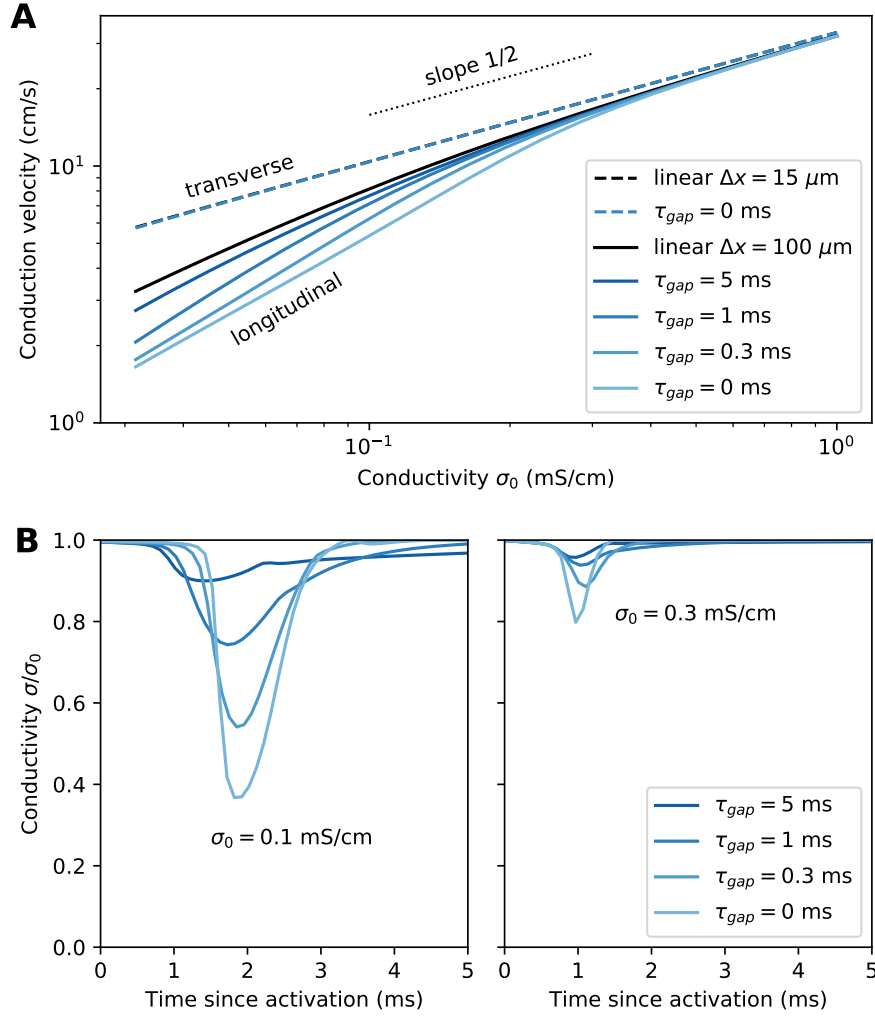
14

FIG. 5. Propagation in one dimension using the Kim cell model with different gap junction model parameters. (A) Conduction velocity as a function of tissue conductivity σ_0 in a cable with discretization $\Delta x = 15\,\mu$m (dashed lines) or $100\,\mu$m (solid lines). The time constant τ_{gap} is color-coded in different shades of blue. The black curves represent simulations with linear gap junctions. The black dashed line ($100\,\mu$m; linear gap junctions) is hidden behind the blue dashed lines ($100\,\mu$m; nonlinear gap junctions). (B) Evolution of the conductivity ratio σ/σ_0 at the midpoint of the cable with $100\,\mu$m resolution for different values of τ_{gap} (color-coded). The baseline conductivity σ_0 is 0.1 mS/cm (left panel) and 0.3 mS/cm (right panel). The time $t = 0$ corresponds to the activation of the cell adjacent of the cable segment for which σ is reported.

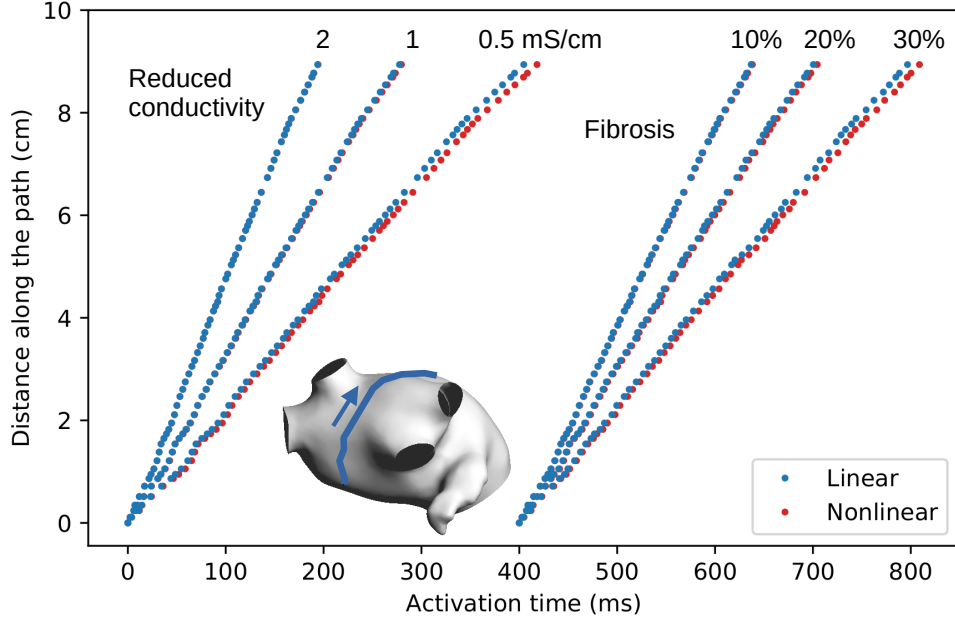stimulus site, as illustrated in Fig. 6.

FIG. 6. Activation times during sinus rhythm along a path from the initiation site and the latest activated site (blue line on the atrial surface). This line follows mostly but not exclusively longitudinal fibers. Activation times in the linear model (blue dots; model L) and in a nonlinear model (red dots; model D_0) are compared. The six substrates with the Kim cell model are represented. For the sake of clarity, the substrates with fibrosis (density indicated above each curve) are shifted by 400 ms with respect to the substrates with reduced coupling (longitudinal conductivity indicated above each curve).

D.   Reentry in two dimensions

To study abnormal propagation in a simple setup, a functional reentry was initiated by creating a spiral-like initial condition[55] in a 10 by 10 cm planar sheet of tissue (100 μm resolution) with a uniform isotropic conductivity of 0.3 mS/cm^2 using the Kim or the Workman cellular model, and either a linear or a nonlinear gap junction model (L and D_0 models from Table I). The area of the square tissue was similar to that of the left atrial model.

Simulated wave dynamics are illustrated in Fig. 7 A–B. With the Workman model (panel A), a single stable spiral wave was observed. Nonlinear gap junctions only resulted in a small time shift of the activation pattern because of the slightly slower conduction velocity measured in the previous subsection. In contrast, the Kim model generated meandering waves and wave breaks. After about 1 s of simulation, a qualitative difference between the linear and the nonlinear gap junction models appeared when a conduction block occurred with the nonlinear model only (panel B). Wave dynamics progressively diverged after that
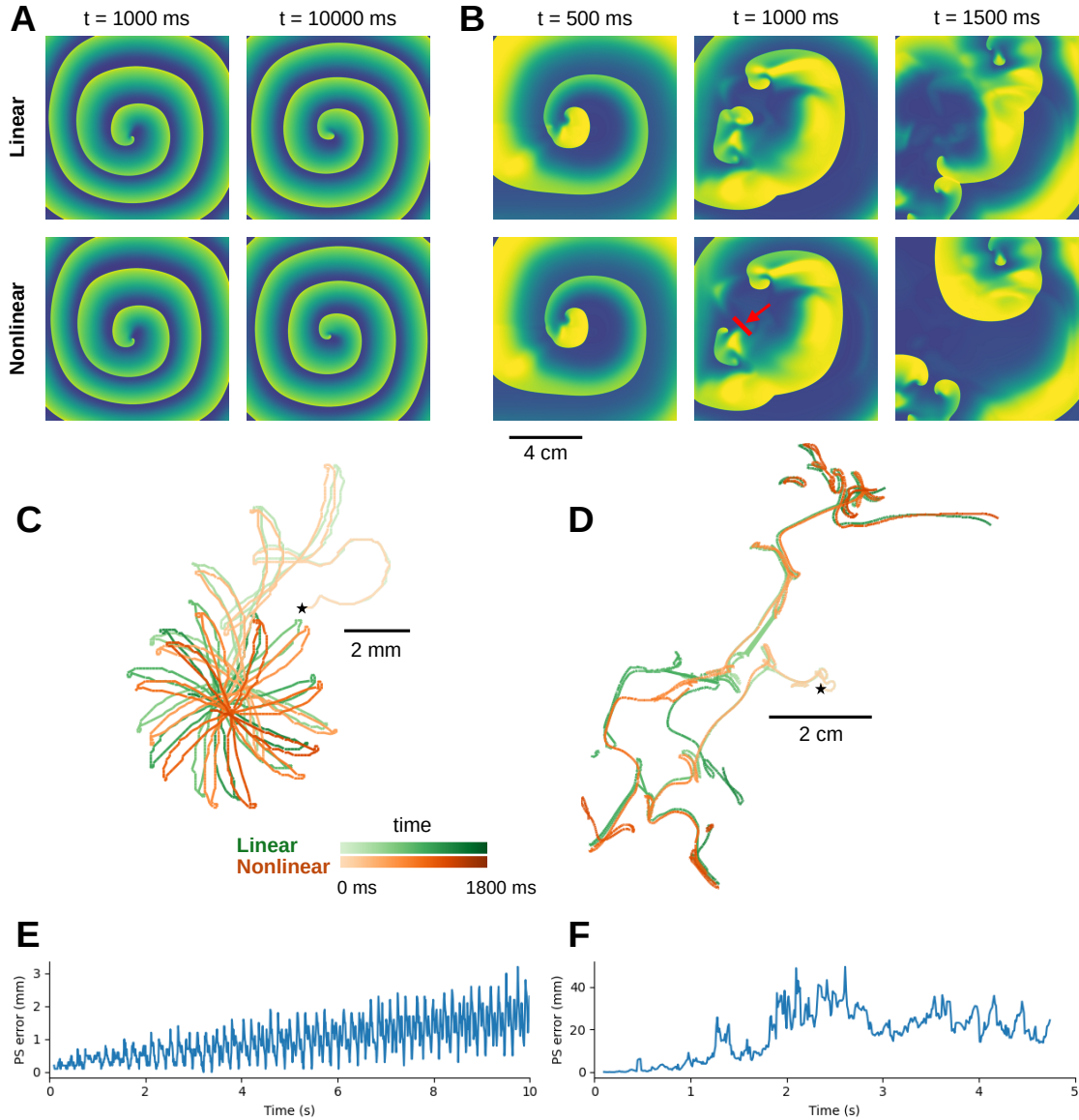
FIG. 7. 2 (A)–(B) Membrane potential maps at different time instants in a 2D model with linear (L; first row) and nonlinear gap junctions (D_0 model; second row) using the Workman model (panel A) or the Kim model (panel B). Membrane potential is color-coded (blue = rest; yellow = depolarized). The red arrow indicates the location of a conduction block not present in the linear gap junction model. (C)–(D) Trajectories of phase singularities during the first 1800 ms of the simulations of reentries of panels (A) and (B) with linear (green curves) and nonlinear (red curves) gap junction models, using the Workman model (panel C) and the Kim model (panel D). The lightness of the color is associated with time evolution. The star denotes the initial phase singularity location. Note the differences in space scales. (E)–(F) Discrepancy in phase singularity location (PS error) between the linear and the nonlinear models with the Workman model (panel E) and the Kim model (panel F). The curve in panel F stops when the reentry self-terminates in the linear model.

event ($t = 1500$ ms).

17

To better describe the phenomena near the core of the reentries, phase singularities were identified and their trajectories were reconstructed,[56] as shown in Fig. 7 C–D. With the Workman model, phase singularity trajectory was flower-like (panel C), the petals being time- or phase-shifted between the linear and nonlinear gap junction models. The Kim model led to more significant differences in trajectories. The fibrillation in the linear model self-terminated after about 5 s while reentries were still present in the nonlinear model after 10 s. Random time to self-termination is indeed a common feature in multiple meandering reentrant wave models of fibrillation.

The discrepancy in phase singularity positions between the linear and nonlinear models was quantified as the root mean square distance between each phase singularity in either model and the nearest one from the other model. When there was only one spiral (Fig. 7 C), this simplified to the distance between the corresponding phase singularities in the two models. The time evolution of that discrepancy is plotted in Fig. 7 E–F. The discrepancy slowly increased with the Workman model (panel E) and eventually became of the order of the size of a petal of the flower-like trajectory (> 2 mm). With the Kim model, after about 1 s of regular increase, the discrepancy jumped to larger values (2–4 cm), demonstrating that the evolution became radically different. On the other hand, the mean number of phase singularities was only slightly larger in the nonlinear model as compared to the linear model (5.46 vs 5.34).

E.   Simulated atrial fibrillation

Examples of AF simulations with linear (L model from Table I) or nonlinear gap junctions (D_0 model) are presented in Fig. 8. The L and D_0 simulations started from the same initial condition (first column of Fig. 8). Because of the slightly slower conduction velocity in the D_0 model, a delay progressively built up (panel A). Ultimately, the delay became sufficient to alter refractoriness and wavefront propagation (panel B, $t = 2400, 3200$ ms). With the Kim cell model featuring steeper restitution, small changes evolved into qualitative differences such as the appearance (panel C, $t = 1610$ ms) or the suppression (panel D, $t = 1670$ ms) of a conduction block, eventually resulting in an apparently uncorrelated wavefront dynamics ($t > 2000$ ms).

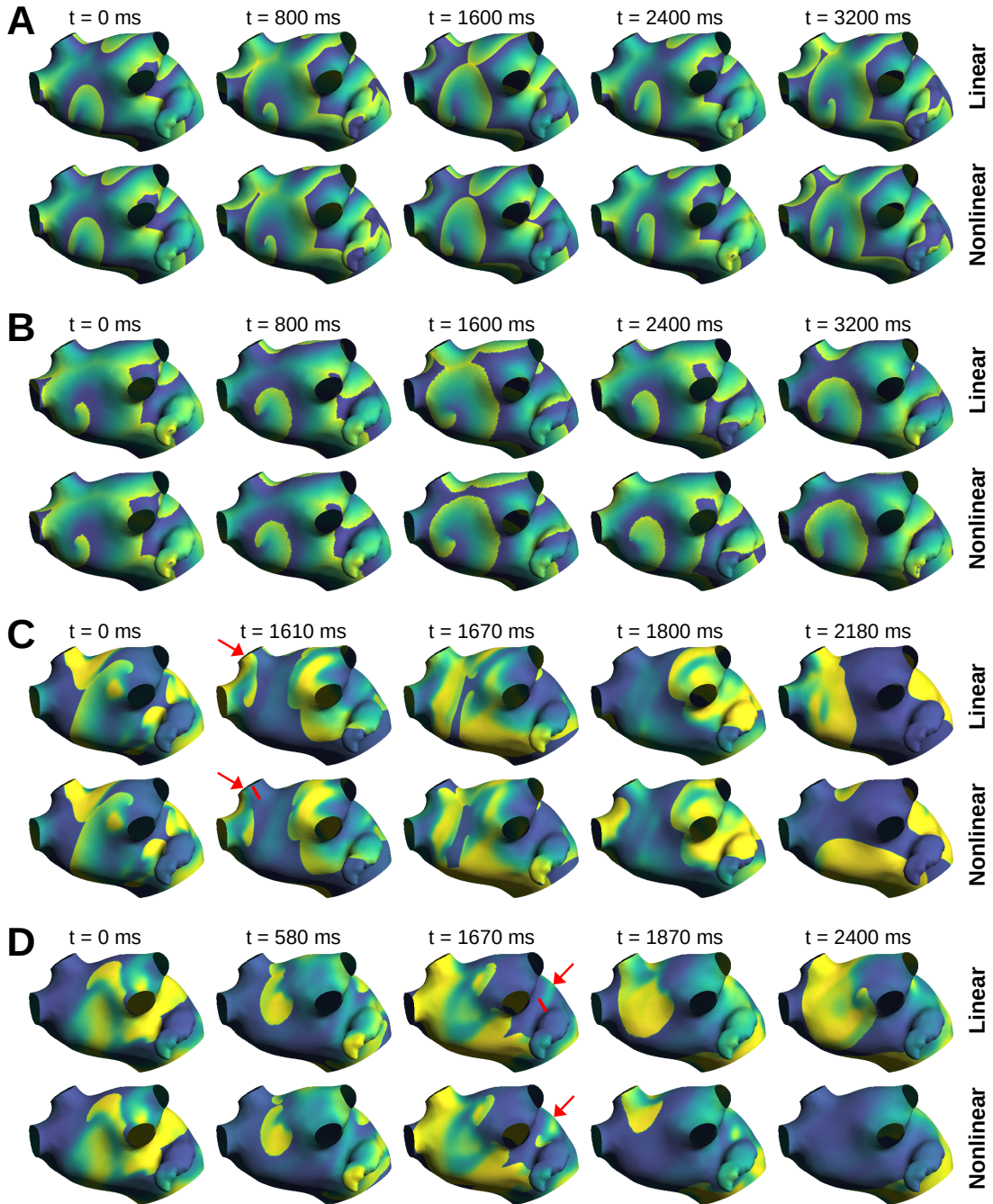Out of 336 AF simulations, 18 self-terminated before 5 s, all with the Kim cellular model

FIG. 8. Membrane potential maps at 5 time instants in models with linear (L; first row of each panel) and nonlinear gap junctions (D_0 model; second row). Membrane potential is color-coded (blue = rest; yellow = depolarized). Red arrows indicate the location of conduction blocks. (A) Workman model with uniform longitudinal conductivity $\sigma_0 = 0.5$ mS/cm; (B) Workman model with 30% fibrosis; (C) Kim model with $\sigma_0 = 1$ mS/cm; (D) Kim model with 20% fibrosis.

and faster CV. Due to the random nature of self-termination, AF duration in models with nonlinear gap junctions were sometimes longer and sometimes shorter than the correspond-

Model	Cycle length (ms)	#Wavelets
Workman model		
Linear	142.2 ± 3.8	2.57 ± 0.63
Nonlinear	142.4 ± 3.9	2.59 ± 0.65
Difference	$p = 0.65$	$p = 0.88$
Kim model		
Linear	254.2 ± 6.67	1.96 ± 0.31
Nonlinear	254.5 ± 5.63	1.96 ± 0.30
Difference	$p = 0.82$	$p = 0.90$

TABLE II. Characteristics of atrial fibrillation dynamics, linear ($n = 24$) vs nonlinear ($n = 144$) gap junction models; p -values from paired t-test between matching simulations.

ing AF episodes in a model with linear gap junctions.

The mean cycle length and the mean number of wavelets (defined as connected regions with membrane potential > -70 mV) were computed in all simulations. These quantities are documented in Table II for the two cell models. The results demonstrate that although the evolution was sometimes diverging in models with linear vs nonlinear gap junctions (e.g., Figs. 8C–D), the statistics of wavefront dynamics remained essentially the same.

F.   Discrepancy in activation time

Figure 9 shows the evolution of the discrepancy in activation time between linear and nonlinear gap junction models. The discrepancy curves were averaged over four AF episodes starting from different initial conditions. The discrepancy increased faster when conduction was slower (third vs first column), whether it was caused by conductivity reduction or by diffuse fibrosis, and was higher with the Kim model (panels G–L) as compared to the Workman model (panels A–F). In the cases with most impaired conduction (panels F, I, L), the discrepancy tended to saturate after 2.5 to 3 s. To get a sense of how much the discrepancy can be expected to grow, the average discrepancy between simulations starting from different, independent initial conditions was computed. The resulting value, displayed as a horizontal dashed line in the figure, was approximately 1/4 of a cycle length. This is explained by the fact that the time delay between mutual nearest neighbors (local discrepancy $|t_i - t_j^{\mathrm{ref}}|$ in Subsect. II H) cannot exceed half a cycle length. This argument indicates that in the substrates of panels I and L, the discrepancy became essentially as high as possible.
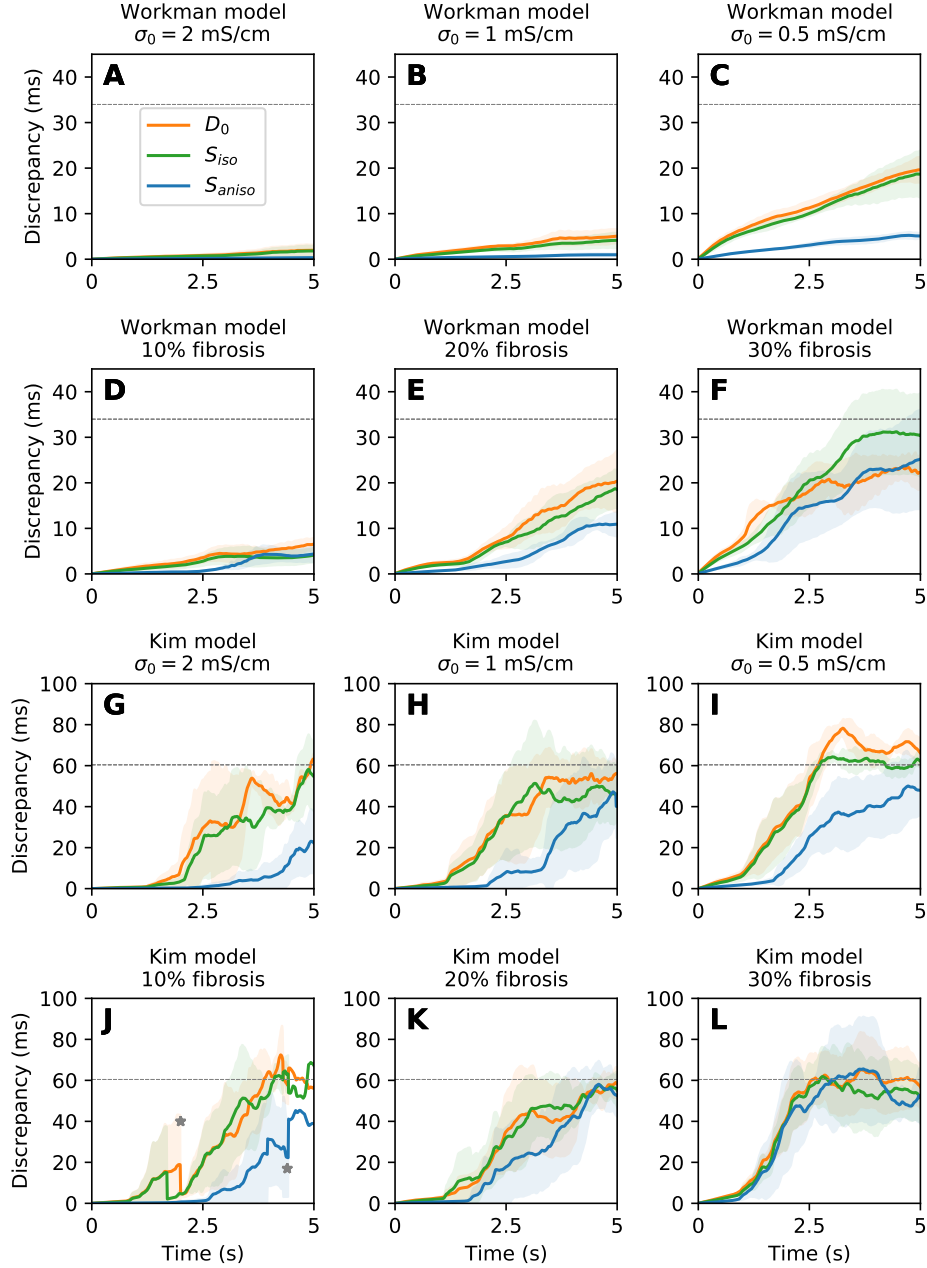
FIG. 9. Time evolution of the discrepancy in activation time between linear and nonlinear gap junction models. Each panel corresponds to a different substrate, described in the title of the panel: (A)–(C) Workman model with reduced conductivity; (D)–(F) Workman model with increasing fibrosis density; (G)–(I) Kim model with reduced conductivity; (J)–(L) Kim model with increasing fibrosis density. Line color represents gap junction models (D_0, S_{iso} and S_{aniso} from Table I). Shaded regions show standard deviations over 4 initial conditions. The dashed horizontal line is the mean discrepancy between two simulations from uncorrelated initial conditions. The gray stars in panel J indicate the time of self-termination of some simulations, which explains the discontinuities in the curves.

Comparison of gap junction models D_0, S_{iso} and S_{aniso} (color-coded in Fig. 9) illustrates
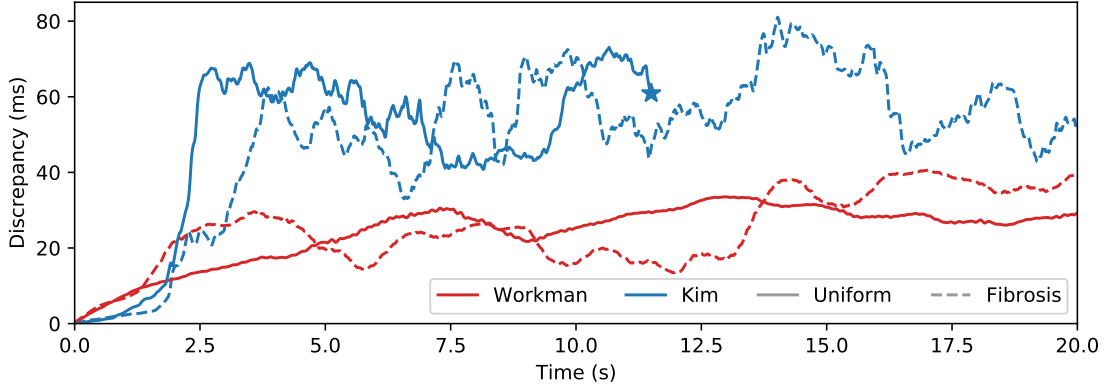
FIG. 10. Time evolution of the discrepancy in activation time between linear and nonlinear gap junction models for the four simulations of Fig. 8 extended to 20 s of fibrillation. The color of the curve refers to the cellular model and the line style to the type of conduction slowing. The star indicates that a fibrillation episode self-terminated.

the effect of scaling the junctional potential. Isotropic scaling to 100 μm (S_{iso}) generally slightly reduced the discrepancy, suggesting that heterogeneity in cell size tended to enhance the nonlinear behavior of gap junctions. Scaling transverse cell size to 15 μm (S_{aniso}) significantly reduced nonlinear diffusion effects. In agreement with Fig. 5, it annihilated almost all transverse effects of gap junction nonlinearity.

To give some insights into the long term behavior of the discrepancy, longer simulations were run for the four substrates of Fig. 8. Figure 10 shows that after a transient phase characterized by a steep increase, the discrepancy fluctuated around its stationary value. With the Workman model, more than 10 s were needed to reach that stationary value.

G. Growth rate of discrepancy

The rate at which the discrepancy increases as a function of time in Fig. 9 was quantified using the growth rate ω. Measured growth rates ranged from 0.06 to 24.1 ms/s. The discrepancy growth rate averaged over all initial conditions and substrates for each cell model was used to compare the gap junction models. Figure 11A confirms that the discrepancy grows faster with the Kim cell model. The effect of scaling the junctional potential appeared to reduce the discrepancy (S_{iso} vs D_0), even more so when the transverse L_{cell} was set to 15 μm (S_{aniso} vs D_0). The time constant τ_{gap} also acted to diminish nonlinear effects ($D_0 > D_2 > D_5 > D_\infty$). However, even when $\tau_{\mathrm{gap}} = \infty$, a residual effect was still present

due to the nonlinearity of the $g_{\mathrm{inst}}(V_j)$ function.

Figure 11B summarizes the differences in discrepancy growth rate among substrates with increasing levels of structural remodeling. The three ranges of CV correspond to the three columns of Fig. 9 in reversed order. Slow conduction substrates were associated with higher discrepancy growth rates.
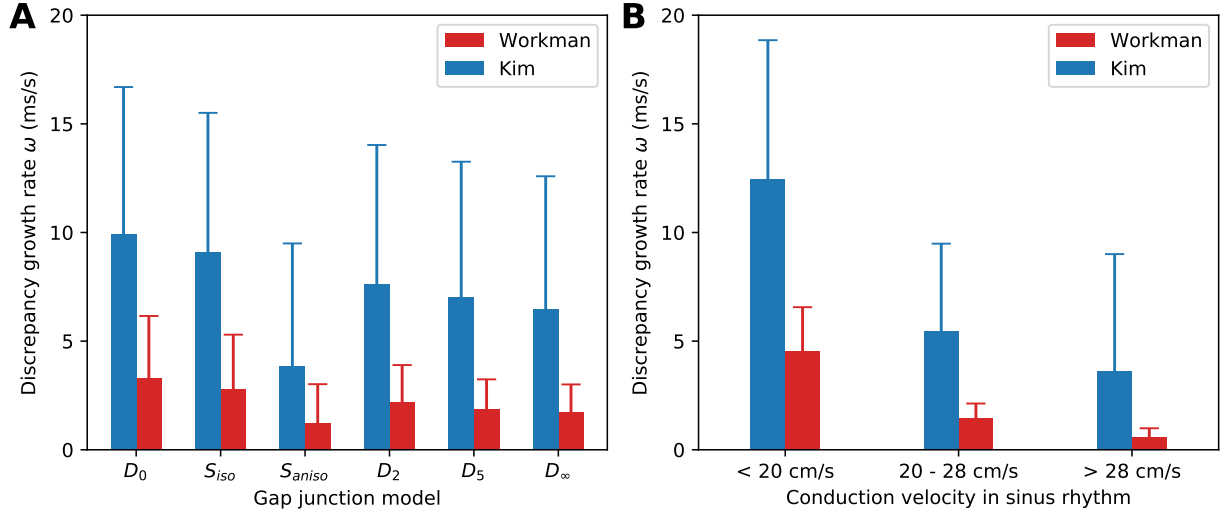

FIG. 11. (A) Discrepancy growth rate for the different gap junction models (code names from Table I) and cell models (color-coded). Bars show mean ± standard deviation over all simulations ($n = 24$). (B) Mean discrepancy growth rate grouped by cell model and conduction velocity during sinus rhythm ($n = 48$ in each of the six groups).

Transverse propagation did not contribute much to the discrepancy in the S_{aniso} gap junction model. We hypothesized that stringy fibrosis would force zigzag propagation and therefore involve longitudinal connections during transverse propagation, which should increase the discrepancy. To test that hypothesis, the simulations using the S_{aniso} model of Fig. 9C (blue curve) served as control (CTL). Stringy fibrosis with average obstacle length of 0.1, 1, 3 and 5 mm and density between 10% and 30% was added and the evolution of the discrepancy was computed for these substrates. Figure 12 shows the resulting discrepancy growth rates. Longer fibrosis obstacles were associated with increased discrepancy growth rates (ANOVA, $p < 0.001$; $n = 20$ per group; excluding CTL). No statistically significant effect of fibrosis density on the discrepancy between linear and nonlinear gap junction models was observed ($p = 0.17$; $n = 12$ per group; excluding CTL). Stringy fibrosis density appeared to affect propagation in linear and nonlinear diffusion models in the same way
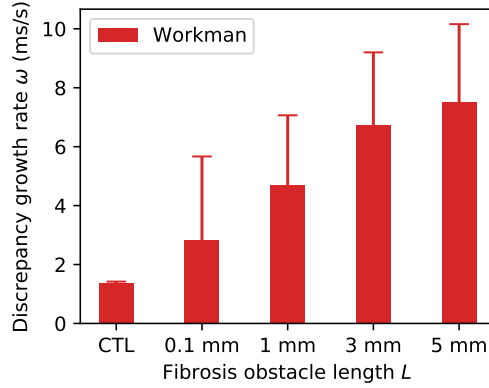
FIG. 12. Discrepancy growth rate in substrates with stringy fibrosis using the Workman cellular model and the S_{aniso} gap junction model. Simulations in substrates with 5 different fibrosis densities are grouped by the average length of the longitudinal obstacles forming the stringy fibrosis model. The control cases (CTL) are substrates without fibrosis. Bars show mean $\pm$ standard deviation over all simulations ($n = 20$).

because only transverse connections were uncoupled.

IV. DISCUSSION

A. Impact of nonlinear gap junctions on propagation

Previous studies have demonstrated that gap junction nonlinearity and gating kinetics cause further conduction slowing, with possible consequences in diseased tissue with impaired conduction.[35,36] We extended the analysis to a 3D model of atrial fibrillation to investigate how these effects can accumulate over time. We created a simplified dynamical model of gap junction based on the Vogel-Weingart model. It enabled us to control the time constant independently from the conductance-voltage relationships. We developed a method to quantify and monitor the discrepancy between simulations with and without gap junction nonlinearity. This method was appropriate when the discrepancy was small and saturated once the difference in activation time became of the order of a quarter the cycle length. To analyze the evolution over longer periods, data assimilation techniques could be explored.[57–59]

The results in sinus rhythm were consistent with one-dimensional models. The effect became measurable when CV was below 20 cm/s. This translated into at most a few milliseconds of delay in the total activation time of the left atrium. This order of magnitude

24

is similar or smaller than the errors in CV typically made by numerical discretization in large-scale models. Moreover, each new beat resets the delay to zero unless the cycle length is close to the refractory period.

During atrial fibrillation, the discrepancy in activation time slowly accumulated, sometimes resulting in qualitative differences between models with linear and nonlinear gap junctions, e.g. presence or absence of a conduction block. The dynamics eventually became uncorrelated after a few seconds of simulation. However, the average quantities that describe AF dynamics such as cycle length and number of wavelets or phase singularities remained essentially the same (Table II). These quantities matter because they are often used for validation or comparison to clinical data.

B.   Factors modulating non-ohmic effects

The magnitude of the effect of gap junction nonlinearity was quantified using the discrepancy growth rate ω. This measure expresses the average accumulation of delay in activation time per second of simulation. The time required to significantly alter the dynamics is of the order of CL/ω, where CL is the cycle length. In our simulations, this time interval varied between a few seconds and tens of seconds.

The factors mitigating non-ohmic effects were:

1. **Normal conduction velocity**: With CV in the range 30 to 40 cm/s or above, the discrepancy growth rate was typically below 5 ms/s (Fig. 11B). Discrepancy was only observed in slow conduction substrates, in agreement with one-dimensional models.[35,36]

2. **Conductivity of the intracellular medium**: Unless propagation was very slow, the intracellular medium contributed to a significant part of the tissue resistivity while exhibiting a linear behavior. As a result, higher cell-to-cell potential differences were needed to create a gap junction-driven dynamic reduction in tissue conductivity (Figs. 4C–D). It could be argued that the linear extracellular conductivity may play a similar role if a bidomain formulation was used.

3. **Small cell size**: The effects were negligible for transverse propagation as shown by the comparison of the S_{iso} vs S_{aniso} model. It was indeed difficult to generate a large

25

potential difference over a distance of 15 μm or shorter. This could also have an impact on models of neonatal cell culture with more spherical, smaller cells.

4. **Time constant of gap junctions**: Once a high junctional potential is established, gates gradually close with a time constant τ_{gap}. When that time delay was larger than the duration of the upstroke phase of the action potential, the non-ohmic effects were limited. However, even when $\tau_{\text{gap}} \to \infty$, a residual effect remained because of the instantaneous conductance-voltage relationship (Fig. 4A). Experimental data from Lin et al.[5] demonstrated the existence of two time constants, a fast one (5 ms, which corresponds to our D_5 model) and a slow one (69 ms, which was practically equivalent to D_∞).

Reciprocally, factors enhancing the non-ohmic effects were:

1. **Conduction heterogeneity**: The discrepancy growth rate tended to be lower in more uniform substrates. This was noticeable in diffuse fibrosis vs uniform reduction in σ_0 (Fig. 9) and in D_0 vs S_{iso} gap junction models (Fig. 11A).

2. **Lateral uncoupling**: Stringy fibrosis forced the involvement of longitudinal gap junctions in transverse propagation due to zigzag pathways (Fig. 12), particularly when obstacle length was larger than the tissue passive space constant. This partly compensated the weakness of non-ohmic effects in transverse gap junctions.

3. **Action potential duration restitution**: The Kim model features a restitution slope close to 1, which increases the sensitivity to the initial condition and creates meandering waves. A small deviation can therefore have a significant impact after a few seconds of fibrillation (Fig. 8). In contrast, relatively stable rotors were observed in the Workman model. Gap junction nonlinearity only caused delayed activation, as illustrated by the linear increase in discrepancy in Figs. 9A–C. Consequently, the discrepancy growth rate is partly caused by the chaotic behavior of the Kim membrane kinetics and not only by the inherent nonlinearity of gap junctions.

C. Implications for cardiac propagation modeling

Our results show that gap junction nonlinearity becomes relevant when CV is of the order of 10 cm/s or slower. Interestingly, this validity limit for the linear diffusion model approximately coincides with the CV below which discrete propagation effects are observed.[60] Such slow conduction has been studied experimentally and numerically in cell strands. Rohr et al. reported a reduced conduction velocity from 36.7 to 0.3 cm/s in a cell strand with severe gap junctional uncoupling.[7] Jousset et al. simulated in a microstructure model propagation slowing below 10 cm/s caused by myofibroblasts.[61] Bruce et al. quantified discrete propagation effects in a numerical model by computing the discrepancy in CV between continuous and discrete models.[19] From 3% at physiologically coupling values, the discrepancy increased to 44% in pathological conditions.

Recent human mapping data suggest that CV is generally > 40 cm/s in patients with atrial fibrillation,[62] although the minimal CV can be as low as 15 to 22 cm/s regionally.[63] In light of these measurements, it does not appear necessary to incorporate dynamic gap junctions in most macroscopic models of atrial fibrillation, even when fibrosis patterns are simulated with locally reduced CV (for instance, 35 to 44 cm/s in Zahid et al.[64] and 40 to 62 in Morgan et al.[65]). Note that despite transverse CV being even slower, the effect of transverse gap junction nonlinearity may be negligible due to cell width.

At a regional level, however, gap junction nonlinearity might play a role. Micro-reentries have been hypothesized to be a mechanism of arrhythmia perpetuation.[66–68] Microstructure models of reentry in very slow conduction zones[69] might benefit from dynamic gap junction models. This would be particularly true in the presence of long activation delays, for instance when propagating though a insert of electrotonically-coupled myofibroblasts.[61]

D. Limitations

A bilayer interconnected cable model was used for several reasons: (1) sustained anatomical and functional reentries can be simulated; (2) longitudinal and transverse connections (and therefore gap junction properties) can be easily identified and labeled; (3) stringy and diffuse fibrosis can be naturally modeled; (4) near-cellular spatial resolution (100 μm) can be reached while keeping computational load reasonable; (5) numerical methods are sufficiently

stable for simulating very slow propagation in a large-scale model; (6) recomputing the whole diffusion matrix is fast enough (it increased computational time by about 45%). Nevertheless, discretization in the transverse direction did not match cell width and variability in cell length (produced by mesh generation[46]) may not be exactly physiological. Scaling potential gradients was therefore needed. The Hurtado et al. homogenization process[36] proved to be a powerful tool for extending the analysis to three dimensions without creating a fully discrete model at cellular resolution.

The diffusion matrix was recomputed every 0.1 ms, which corresponded to the operator-splitting time step.[46] While this time step was certainly appropriate for $\tau_{gap} \geq 1$ ms, the effects of discretization was visible on Fig. 5B when $\tau_{gap} = 0$ ms. This limit case is in itself an approximation since experimental values of τ_{gap} tend to be of the order of at least 5 ms.[5] Note that the conductance is a direct function of the membrane potentials (when $\tau_{gap} = 0$ ms). Since the instantaneous feedback effect of that conductance on membrane potentials is expected to be very small, the accumulation of errors over one cycle remains limited.

Very low coupling between adjacent anatomical structures such as fiber bundles (not present in our model) might enhance non-ohmic effects, notably in the right atrium and the appendages. Despite the lack of full three-dimensional structures, the two layers still allowed between-layer pathways. This topological property is critical in the presence of stringy fibrosis (propagation below or above an obstacle). Changes in inter-layer coupling were not investigated; endo-epicardial delays were very small. This could be another avenue for gap junction nonlinearity to affect propagation.

The lack of an extracellular domain prevented the estimation of three effects. First, the linearity of extracellular diffusion might reduce the nonlinearity of conduction. Second, the interstitial space may also play a role in conduction[70,71] and affect the accuracy of the homogenization process [Eq. (13)]. Third, both gap junction nonlinearity and ephaptic conduction[38,39] become significant when electrical coupling is weak. There may be an interplay between the two.

Two Courtemanche-based cellular models were used, one with a steep and one with a flat restitution to generate both stable and meandering reentries. More sophisticated Markov models of the Na^+ current, channel mutation or sodium blockade might influence the results, as well as calcium-based depolarization like in cardiac nodal cells. Our simplified

gap junction model was based on connexin 40 data.[8] Models of different types of connexins, heterotypic junctions[36] or connexin mutation[72] may further decrease conduction velocity, although we would expect the discrepancy growth rates to be of the same order of magnitude.

Uniform fibrosis or slow conduction was specified in the entire atrial surface to reduce the number of parameters. More realistic models of arrhythmogenic substrates would include heterogeneous fibrosis distribution, where regions of slow conduction and lesions delimit critical pathways for the maintenance of the reentries.[73,74] This might lead to stronger, but more localized non-ohmic effects.

V. CONCLUSION

Our simulation results shed light on the validity range and potential limitations of the linear approximation for the current-voltage relationship of gap junctions for its use in large-scale anatomical models. During sinus rhythm in a substrate with moderate structural remodeling, the discrepancy in activation time remained within the margin of error of the numerical methods. During atrial fibrillation, the discrepancy slowly accumulated and eventually reached the point where linear and nonlinear gap junction models led to two different episodes of the same arrhythmia. Significant non-ohmic effects were observed in very slow conduction regions (< 10 cm/s), with potential impact on the simulation of microreentries and critical pathways in heterogeneous fibrotic substrates. The time scales involved (5–10 s) motivate the simulation of longer episodes with statistical analysis of spatiotemporal complexity indices.[75,76] Moreover, accumulation of small nonlinearities over time may generate complex patterns of action potential alternans and contribute to the occurrence of conduction blocks and wavebreaks.[23,77] This advocates for further development of nonlinear, multiscale, multiphysics, non-local approaches to simulate the complex route to arrhythmia.

CONFLICT OF INTEREST

The authors have no conflict of interest to disclose.

DATA AVAILABILITY STATEMENT

The data that support the findings of this study are available from the corresponding author upon reasonable request.

REFERENCES

[1] S. Weidmann, "The diffusion of radiopotassium across intercalated disks of mammalian cardiac muscle," *The Journal of Physiology*, vol. 187, pp. 323–342, Nov. 1966.

[2] M. S. Nielsen, L. N. Axelsen, P. L. Sorgen, V. Verma, M. Delmar, and N.-H. Holstein-Rathlou, "Gap Junctions," *Comprehensive Physiology*, vol. 2, p. 10.1002/cphy.c110051, July 2012.

[3] R. G. Gourdie, C. R. Green, and N. J. Severs, "Gap junction distribution in adult mammalian myocardium revealed by an anti-peptide antibody and laser scanning confocal microscopy," *Journal of Cell Science*, vol. 99 (Pt 1), pp. 41–55, May 1991.

[4] A. G. Kléber and Y. Rudy, "Basic mechanisms of cardiac impulse propagation and associated arrhythmias," *Physiological Reviews*, vol. 84, pp. 431–488, Apr. 2004.

[5] X. Lin, J. Gemel, A. Glass, C. W. Zemlin, E. C. Beyer, and R. D. Veenstra, "Connexin40 and connexin43 determine gating properties of atrial gap junction channels," *Journal of molecular and cellular cardiology*, vol. 48, p. 238, Jan. 2010.

[6] R. H. Hoyt, M. L. Cohen, and J. E. Saffitz, "Distribution and three-dimensional structure of intercellular junctions in canine myocardium," *Circulation Research*, vol. 64, pp. 563–574, Mar. 1989.

[7] S. Rohr, "Role of gap junctions in the propagation of the cardiac action potential," *Cardiovascular Research*, vol. 62, pp. 309–322, May 2004.

[8] T. R. Brown, T. Krogh-Madsen, and D. J. Christini, "Illuminating myocyte-fibroblast homotypic and heterotypic gap junction dynamics using dynamic clamp," *Biophysical Journal*, vol. 111, pp. 785–797, Aug. 2016.

[9] H. J. Jongsma and R. Wilders, "Gap junctions in cardiovascular disease," *Circulation Research*, vol. 86, pp. 1193–1197, June 2000.

[10] S. Dhein, *Cardiac gap junctions: physiology, regulation, pathophysiology, and pharmacology.* Karger Medical and Scientific Publishers, 1998.

[11] J. H. Smith, C. R. Green, N. S. Peters, S. Rothery, and N. J. Severs, "Altered patterns of gap junction distribution in ischemic heart disease. An immunohistochemical study of human myocardium using laser scanning confocal microscopy," *The American Journal of Pathology*, vol. 139, pp. 801–821, Oct. 1991.

[12] A. L. Wit and N. S. Peters, "The role of gap junctions in the arrhythmias of ischemia and infarction," *Heart Rhythm*, vol. 9, pp. 308–311, Feb. 2012.

[13] N. S. Peters, C. R. Green, P. A. Poole-Wilson, and N. J. Severs, "Cardiac arrhythmogenesis and the gap junction," *Journal of Molecular and Cellular Cardiology*, vol. 27, pp. 37–44, Jan. 1995.

[14] M. S. Spach, J. F. Heidlage, P. C. Dolber, and R. C. Barr, "Electrophysiological effects of remodeling cardiac gap junctions and cell size: experimental and model studies of normal cardiac growth," *Circulation Research*, vol. 86, pp. 302–311, Feb. 2000.

[15] N. J. Severs, A. F. Bruce, E. Dupont, and S. Rothery, "Remodelling of gap junctions and connexin expression in diseased myocardium," *Cardiovascular Research*, vol. 80, pp. 9–19, Oct. 2008.

[16] J. C. Neu and W. Krassowska, "Homogenization of syncytial tissues," *Critical Reviews in Biomedical Engineering*, vol. 21, no. 2, pp. 137–199, 1993.

[17] P. E. Hand and C. S. Peskin, "Homogenization of an electrophysiological model for a strand of cardiac myocytes with gap-junctional and electric-field coupling," *Bulletin of Mathematical Biology*, vol. 72, pp. 1408–1424, Aug. 2010.

[18] B. A. J. Lawson, R. W. d. Santos, I. W. Turner, A. Bueno-Orovio, P. Burrage, and K. Burrage, "Homogenisation for the monodomain model in the presence of microscopic fibrotic structures," *arXiv:2012.05527 [physics]*, Dec. 2020. arXiv: 2012.05527.

[19] D. Bruce, P. Pathmanathan, and J. P. Whiteley, "Modelling the effect of gap junctions on tissue-level cardiac electrophysiology," *Bulletin of Mathematical Biology*, vol. 76, pp. 431–454, Feb. 2014.

[20] R. Vogel and R. Weingart, "Mathematical model of vertebrate gap junctions derived from electrical measurements on homotypic and heterotypic channels," *The Journal of Physiol-*

ogy, vol. 510, pp. 177–189, July 1998.

[21] A. Bueno-Orovio, D. Kay, V. Grau, B. Rodriguez, and K. Burrage, "Fractional diffusion models of cardiac electrical propagation: role of structural heterogeneity in dispersion of repolarization," *Journal of the Royal Society, Interface*, vol. 11, p. 20140352, Aug. 2014.

[22] N. Cusimano, A. Gizzi, F. H. Fenton, S. Filippi, and L. Gerardo-Giorda, "Key aspects for effective mathematical modelling of fractional-diffusion in cardiac electrophysiology: A quantitative study," *Communications in Nonlinear Science and Numerical Simulation*, vol. 84, p. 105152, May 2020.

[23] N. Cusimano, L. Gerardo-Giorda, and A. Gizzi, "A space-fractional bidomain framework for cardiac electrophysiology: 1D alternans dynamics," *Chaos (Woodbury, N.Y.)*, vol. 31, p. 073123, July 2021.

[24] D. E. Hurtado, S. Castro, and A. Gizzi, "Computational modeling of non-linear diffusion in cardiac electrophysiology: A novel porous-medium approach," *Computer Methods in Applied Mechanics and Engineering*, vol. 300, pp. 70–83, 2016.

[25] C. Cherubini, S. Filippi, A. Gizzi, and R. Ruiz-Baier, "A note on stress-driven anisotropic diffusion and its role in active deformable media," *Journal of Theoretical Biology*, vol. 430, pp. 221–228, Oct. 2017.

[26] P. Lenarda, A. Gizzi, and M. Paggi, "A modeling framework for electro-mechanical interaction between excitable deformable cells," *European Journal of Mechanics - A/Solids*, vol. 72, pp. 374–392, Nov. 2018.

[27] A. Loppini, A. Gizzi, R. Ruiz-Baier, C. Cherubini, F. H. Fenton, and S. Filippi, "Competing Mechanisms of Stress-Assisted Diffusivity and Stretch-Activated Currents in Cardiac Electromechanics," *Frontiers in Physiology*, vol. 9, 2018.

[28] A. Gizzi, A. Loppini, R. Ruiz-Baier, A. Ippolito, A. Camassa, A. La Camera, E. Emmi, L. Di Perna, V. Garofalo, C. Cherubini, and S. Filippi, "Nonlinear diffusion and thermo-electric coupling in a two-variable model of cardiac action potential," *Chaos (Woodbury, N.Y.)*, vol. 27, p. 093919, Sept. 2017.

[29] F. H. Fenton, A. Gizzi, C. Cherubini, N. Pomella, and S. Filippi, "Role of temperature on nonlinear cardiac dynamics," *Physical Review. E, Statistical, Nonlinear, and Soft Matter Physics*, vol. 87, p. 042717, Apr. 2013.

[30] A. Loppini, A. Barone, A. Gizzi, C. Cherubini, F. H. Fenton, and S. Filippi, "Thermal effects on cardiac alternans onset and development: A spatiotemporal correlation analysis,"

Physical Review E, vol. 103, p. L040201, Apr. 2021.

[31] M. Snipas, T. Kraujalis, K. Maciunas, L. Kraujaliene, L. Gudaitis, and V. K. Verselis, "Four-State Model for Simulating Kinetic and Steady-State Voltage-Dependent Gating of Gap Junctions," *Biophysical Journal*, vol. 119, pp. 1640–1655, Oct. 2020.

[32] Y. Chen-Izu, A. P. Moreno, and R. A. Spangler, "Opposing gates model for voltage gating of gap junction channels," *American Journal of Physiology. Cell Physiology*, vol. 281, pp. C1604–1613, Nov. 2001.

[33] X. Lin, J. Gemel, E. C. Beyer, and R. D. Veenstra, "Dynamic model for ventricular junctional conductance during the cardiac action potential," *American journal of physiology. Heart and circulatory physiology*, vol. 288, pp. H1113–H1123, Mar. 2005.

[34] C. Oka, H. Matsuda, N. Sarai, and A. Noma, "Modeling the calcium gate of cardiac gap junction channel," *The journal of physiological sciences: JPS*, vol. 56, pp. 79–85, Feb. 2006.

[35] A. P. Henriquez, R. Vogel, B. J. Muller-Borer, C. S. Henriquez, R. Weingart, and W. E. Cascio, "Influence of dynamic gap junction resistance on impulse propagation in ventricular myocardium: a computer simulation study.," *Biophysical Journal*, vol. 81, pp. 2112–2121, Oct. 2001.

[36] D. E. Hurtado, J. Jilberto, and G. Panasenko, "Non-ohmic tissue conduction in cardiac electrophysiology: Upscaling the non-linear voltage-dependent conductance of gap junctions," *PLOS Computational Biology*, vol. 16, p. e1007232, Feb. 2020.

[37] K. H. Jæger, A. G. Edwards, A. McCulloch, and A. Tveito, "Properties of cardiac conduction in a cell-based computational model," *PLOS Computational Biology*, vol. 15, p. e1007042, May 2019.

[38] S. H. Weinberg, "Ephaptic coupling rescues conduction failure in weakly coupled cardiac tissue with voltage-gated gap junctions," *Chaos: An Interdisciplinary Journal of Nonlinear Science*, vol. 27, p. 093908, Sept. 2017.

[39] J. Lin and J. P. Keener, "Modeling electrical activity of myocardial cells incorporating the effects of ephaptic coupling," *Proceedings of the National Academy of Sciences of the United States of America*, vol. 107, pp. 20935–20940, Dec. 2010.

[40] P.-E. Bécue, M. Potse, and Y. Coudière, "A three-dimensional computational model of action potential propagation through a network of individual cells," in *2017 Computing in Cardiology*, p. 057, 2017.

[41] P.-E. Bécue, M. Potse, and Y. Coudière, "Microscopic simulation of the cardiac electro-physiology: A study of the influence of different gap junctions models," in *2018 Computing in Cardiology Conference*, vol. 45, pp. 022–271, 2018.

[42] L. M. Treml, E. Bartocci, and A. Gizzi, "Modeling and Analysis of Cardiac Hybrid Cellular Automata via GPU-Accelerated Monte Carlo Simulation," *Mathematics*, vol. 9, p. 164, Jan. 2021.

[43] A. Kaboudian, E. M. Cherry, and F. H. Fenton, "Real-time interactive simulations of large-scale systems on personal computers and cell phones: Toward patient-specific heart modeling and other applications," *Science Advances*, vol. 5, p. eaav6019, Mar. 2019.

[44] X. Lin, C. Zemlin, J. K. Hennan, J. S. Petersen, and R. D. Veenstra, "Enhancement of ventricular gap-junction coupling by rotigaptide," *Cardiovascular Research*, vol. 79, pp. 416–426, Aug. 2008.

[45] A. Saliani, A. Tsikhanovich, and V. Jacquemet, "Visualization of interpolated atrial fiber orientation using evenly-spaced streamlines," *Comput Biol Med*, vol. 111, p. 103349, 2019.

[46] A. Saliani and V. Jacquemet, "Diffuse and stringy fibrosis in a bilayer interconnected cable model of the left atrium," *Computing in Cardiology*, vol. 47, 2020.

[47] A. Saliani, E. Irakoze, and V. Jacquemet, "Simulation of diffuse and stringy fibrosis in a bilayer interconnected cable model of the left atrium," *EP Europace*, vol. 23, pp. i169–i177, Mar. 2021.

[48] J. P. Kucera, S. Rohr, and Y. Rudy, "Localization of sodium channels in intercalated disks modulates cardiac conduction," *Circulation Research*, vol. 91, pp. 1176–1182, Dec. 2002.

[49] M. Courtemanche, R. J. Ramirez, and S. Nattel, "Ionic targets for drug therapy and atrial fibrillation-induced electrical remodeling: insights from a mathematical model," *Cardiovascular Research*, vol. 42, pp. 477–489, May 1999.

[50] A. J. Workman, K. A. Kane, and A. C. Rankin, "The contribution of ionic currents to changes in refractoriness of human atrial myocytes associated with chronic atrial fibrillation," *Cardiovascular Research*, vol. 52, pp. 226–235, Nov. 2001.

[51] V. Jacquemet, N. Virag, Z. Ihara, L. Dang, O. Blanc, S. Zozor, J.-M. Vesin, L. Kappenberger, and C. Henriquez, "Study of unipolar electrogram morphology in a computer model of atrial fibrillation," *Journal of Cardiovascular Electrophysiology*, vol. 14, pp. S172–179, Oct. 2003.

[52] B.-S. Kim, Y.-H. Kim, G.-S. Hwang, H.-N. Pak, S. C. Lee, W. J. Shim, D. J. Oh, and Y. M. Ro, "Action potential duration restitution kinetics in human atrial fibrillation," *Journal of the American College of Cardiology*, vol. 39, pp. 1329–1336, Apr. 2002.

[53] S. Labarthe, J. Bayer, Y. Coudière, J. Henry, H. Cochet, P. Jaïs, and E. Vigmond, "A bilayer model of human atria: Mathematical background, construction, and assessment," *EP Europace*, vol. 16 Suppl 4, pp. iv21–iv29, 2014.

[54] A. Herlin and V. Jacquemet, "Eikonal-based initiation of fibrillatory activity in thin-walled cardiac propagation models," *Chaos (Woodbury, N.Y.)*, vol. 21, p. 043136, Dec. 2011.

[55] A. Herlin and V. Jacquemet, "Reconstruction of phase maps from the configuration of phase singularities in two-dimensional manifolds," *Physical Review. E, Statistical, Nonlinear, and Soft Matter Physics*, vol. 85, p. 051916, May 2012.

[56] S. Gagné and V. Jacquemet, "Time resolution for wavefront and phase singularity tracking using activation maps in cardiac propagation models," *Chaos (Woodbury, N.Y.)*, vol. 30, p. 033132, Mar. 2020.

[57] P. Pathmanathan, S. K. Galappaththige, J. M. Cordeiro, A. Kaboudian, F. H. Fenton, and R. A. Gray, "Data-Driven Uncertainty Quantification for Cardiac Electrophysiological Models: Impact of Physiological Variability on Action Potential and Spiral Wave Dynamics," *Frontiers in Physiology*, vol. 11, 2020.

[58] C. D. Marcotte, F. H. Fenton, M. J. Hoffman, and E. M. Cherry, "Robust data assimilation with noise: Applications to cardiac dynamics," *Chaos: An Interdisciplinary Journal of Nonlinear Science*, vol. 31, p. 013118, Jan. 2021.

[59] A. Barone, A. Gizzi, F. Fenton, S. Filippi, and A. Veneziani, "Experimental validation of a variational data assimilation procedure for estimating space-dependent cardiac conductivities," *Computer Methods in Applied Mechanics and Engineering*, vol. 358, p. 112615, Jan. 2020.

[60] Y. Rudy and W. L. Quan, "A model study of the effects of the discrete cellular structure on electrical propagation in cardiac tissue," *Circulation Research*, vol. 61, pp. 815–823, Dec. 1987.

[61] F. Jousset, A. Maguy, S. Rohr, and J. P. Kucera, "Myofibroblasts Electrotonically Coupled to Cardiomyocytes Alter Conduction: Insights at the Cellular Level from a Detailed In silico Tissue Structure Model," *Frontiers in Physiology*, vol. 7, p. 496, Oct. 2016.

[62] W. F. B. van der Does, C. A. Houck, A. Heida, M. S. van Schie, F. R. N. van Schaagen, Y. J. H. J. Taverne, A. J. J. C. Bogers, and N. M. S. de Groot, "Atrial electrophysiological characteristics of aging," *Journal of Cardiovascular Electrophysiology*, vol. 32, pp. 903–912, Apr. 2021.

[63] A. Heida, M. S. van Schie, W. F. B. van der Does, Y. J. H. J. Taverne, A. J. J. C. Bogers, and N. M. S. de Groot, "Reduction of conduction velocity in patients with atrial fibrillation," *Journal of Clinical Medicine*, vol. 10, p. 2614, June 2021.

[64] S. Zahid, H. Cochet, P. M. Boyle, E. L. Schwarz, K. N. Whyte, E. J. Vigmond, R. Dubois, M. Hocini, M. Haïssaguerre, P. Jaïs, and N. A. Trayanova, "Patient-derived models link re-entrant driver localization in atrial fibrillation to fibrosis spatial pattern," *Cardiovascular Research*, vol. 110, pp. 443–454, June 2016.

[65] R. Morgan, M. A. Colman, H. Chubb, G. Seemann, and O. V. Aslanidi, "Slow Conduction in the Border Zones of Patchy Fibrosis Stabilizes the Drivers for Atrial Fibrillation: Insights from Multi-Scale Human Atrial Modeling," *Frontiers in Physiology*, vol. 7, p. 474, 2016.

[66] B. J. Hansen, J. Zhao, T. A. Csepe, B. T. Moore, N. Li, L. A. Jayne, A. Kalyanasundaram, P. Lim, A. Bratasz, K. A. Powell, O. P. Simonetti, R. S. D. Higgins, A. Kilic, P. J. Mohler, P. M. L. Janssen, R. Weiss, J. D. Hummel, and V. V. Fedorov, "Atrial fibrillation driven by micro-anatomic intramural re-entry revealed by simultaneous sub-epicardial and sub-endocardial optical mapping in explanted human hearts," *European Heart Journal*, vol. 36, pp. 2390–2401, Sept. 2015.

[67] F. S. Ng, F. Guerrero, V. Luther, M. Sikkel, and P. B. Lim, "Microreentrant left atrial tachycardia circuit mapped with an ultra-high-density mapping system," *HeartRhythm Case Reports*, vol. 3, pp. 224–228, Apr. 2017.

[68] E. M. Cherry, J. R. Ehrlich, S. Nattel, and F. H. Fenton, "Pulmonary vein reentry–properties and size matter: insights from a computational analysis," *Heart Rhythm*, vol. 4, pp. 1553–1562, Dec. 2007.

[69] M. L. Hubbard and C. S. Henriquez, "A microstructural model of reentry arising from focal breakthrough at sites of source-load mismatch in a central region of slow conduction," *American Journal of Physiology - Heart and Circulatory Physiology*, vol. 306, pp. H1341–H1352, May 2014.

[70] S. F. Roberts, J. G. Stinstra, and C. S. Henriquez, "Effect of Nonuniform Interstitial Space Properties on Impulse Propagation: A Discrete Multidomain Model," *Biophysical Journal*,

vol. 95, pp. 3724–3737, Oct. 2008.

[71] M. L. Hubbard and C. S. Henriquez, "Increased interstitial loading reduces the effect of microstructural variations in cardiac tissue," *American Journal of Physiology. Heart and Circulatory Physiology*, vol. 298, pp. H1209–1218, Apr. 2010.

[72] I. Lübkemeier, R. Andrié, L. Lickfett, F. Bosen, F. Stöckigt, R. Dobrowolski, A. M. Draffehn, J. Fregeac, J. L. Schultze, F. F. Bukauskas, J. W. Schrickel, and K. Willecke, "The Connexin40A96S mutation from a patient with atrial fibrillation causes decreased atrial conduction velocities and sustained episodes of induced atrial fibrillation in mice," *Journal of Molecular and Cellular Cardiology*, vol. 65, pp. 19–32, Dec. 2013.

[73] P. M. Boyle, S. Zahid, and N. A. Trayanova, "Towards personalized computational modelling of the fibrotic substrate for atrial arrhythmia," *EP Europace*, vol. 18, pp. iv136–iv145, Dec. 2016.

[74] C. H. Roney, J. D. Bayer, S. Zahid, M. Meo, P. M. J. Boyle, N. A. Trayanova, M. Haïssaguerre, R. Dubois, H. Cochet, and E. J. Vigmond, "Modelling methodology of atrial fibrosis affects rotor dynamics and electrograms," *EP Europace*, vol. 18, pp. iv146–iv155, Dec. 2016.

[75] W. A. Ramírez, A. Gizzi, K. L. Sack, S. Filippi, J. M. Guccione, and D. E. Hurtado, "On the Role of Ionic Modeling on the Signature of Cardiac Arrhythmias for Healthy and Diseased Hearts," *Mathematics*, vol. 8, p. 2242, Dec. 2020.

[76] M. Hörning, F. Blanchard, A. Isomura, and K. Yoshikawa, "Dynamics of spatiotemporal line defects and chaos control in complex excitable systems," *Scientific Reports*, vol. 7, p. 7757, Aug. 2017.

[77] A. Gizzi, E. Cherry, R. Gilmour, S. Luther, S. Filippi, and F. Fenton, "Effects of Pacing Site and Stimulation History on Alternans Dynamics and the Development of Complex Spatiotemporal Patterns in Cardiac Tissue," *Frontiers in Physiology*, vol. 4, 2013.

37